

# A novel approach of divergence-free reconstruction for adaptive mesh refinement

Shengtai Li <sup>a,\*</sup>, Hui Li <sup>b</sup>

<sup>a</sup> *Theoretical Division, MS B284, Los Alamos National Laboratory, Los Alamos, NM 87545, USA*

<sup>b</sup> *Applied Physics Division, MS B288, Los Alamos National Laboratory, Los Alamos, NM 87545, USA*

Received 8 May 2003; received in revised form 27 November 2003; accepted 28 January 2004

Available online 17 March 2004

## Abstract

A simple novel approach to maintain the divergence-free condition with adaptive mesh refinement is presented. This new approach uses reconstructions on the coarse faces together with the divergence-free condition to reconstruct the field values on the internal fine faces. It does not construct a global interpolation polynomial over a whole coarse cell. Therefore, it can be easily applied to any refinement ratio. It is implemented via a directionally splitting approach so that it can be applied to any kind of grids and in any dimensions. Implementation is presented in the Cartesian, cylindrical and spherical geometries. It is shown by several 2D magneto-hydrodynamic simulations that such a method can keep the divergence-free error of magnetic fields at the round-off level.

© 2004 Elsevier Inc. All rights reserved.

**Keywords:** Adaptive mesh refinement; Divergence-free; Magnetohydrodynamics; Cylindrical geometry; Spherical geometry; Finite volume method

## 1. Introduction

Adaptive and hierarchical grids provide some of the most efficient spatial discretization for multi-scale computational problems. It is of great interest to extend numerical schemes designed for a simple structured mesh to adaptive and hierarchical grids. It is critical to conserve the properties of solutions when the mesh resolution changes. Berger and Colella [1] proposed an adaptive mesh refinement (AMR) scheme for hydrodynamics to conserve scalar quantities (e.g., mass, energy) and numerical fluxes. Additional challenges, however, are presented in physical systems satisfying the Stokes's law type of equation with the divergence-free evolution of vector fields, such as velocity fields in incompressible hydrodynamics and magnetic fields in magnetohydrodynamics (MHD).

\* Corresponding author. Tel.: +505665-8407; fax: +505665-5757.

E-mail addresses: [sli@lanl.gov](mailto:sli@lanl.gov) (S. Li), [hli@lanl.gov](mailto:hli@lanl.gov) (H. Li).

The divergence-free evolution of magnetic fields is an important issue in developing an MHD code even for a single non-adaptive grid. Brackbill and Barnes [3] have shown that the discretization error with respect to the divergence of the magnetic field ( $\nabla \cdot \mathbf{B}$ ) usually grows exponentially during the computations, causing an artificial force parallel to the magnetic field and destroying the correctness of the solutions. Several approaches have been proposed to handle this problem. Different methods have different advantages and limitations, especially for MHD codes with AMR and parallelization. For example, the *projection method* proposed in [3] has been widely used by many authors (e.g., [12]). However, this method involves solving a Poisson equation, which becomes difficult to implement on an AMR grid and has poor scalability for parallel AMR computation.

Powell et al. [16] used a scheme of Powell [15] by adding a source term that is proportional to  $\nabla \cdot \mathbf{B}$  to the original set of MHD equations. They then argue that this non-physical source term will be advected away and out of the computational box. This approach leads to a Riemann problem which has an eight-wave structure, which is easy to carry over to AMR because all the variables reside at the cell-center. Recently, Janhunen [11] proposed to only add the  $\nabla \cdot \mathbf{B}$  source term to the induction equation, which restores the momentum and energy conservation. Yet another approach has been proposed by Dedner et al. [9] to damp the divergence errors while convecting it away by adding diffusion to the hyperbolic convection of the  $\nabla \cdot \mathbf{B}$ . However, Tóth [18] pointed out that the eight-wave formulation can lead to incorrect jump conditions across strong shocks in the numerical solutions.

Another way to keep  $\nabla \cdot \mathbf{B}$  exactly zero is to rewrite the MHD equations in terms of vector potential  $\mathbf{A}$  and define the magnetic field as  $\mathbf{B} = \nabla \times \mathbf{A}$ . A disadvantage of this approach is that the order of spatial derivatives increases by one, which reduces the order of accuracy by one (see [10] for more details).

The *constrained transport* (CT) method by Evans and Hawley [10] is another approach to keep  $\nabla \cdot \mathbf{B}$  to the accuracy of machine round-off error. This approach has been combined with various shock-capturing schemes by many authors [2,7,8,13,17]. The original CT method used a staggered grid which places the magnetic field variables at the face center and the rest at the cell-center. The divergence-free finite-difference scheme can be easily constructed for the staggered grid (see [20]). Tóth [18] introduced a finite-volume interpretation of the CT schemes that place all of the variables at the cell center. However, this idea is difficult to generalize to an AMR grid.

Several recent studies by Balsara [4] and Tóth and Roe [19] have addressed the question of preserving the divergence-free condition when the mesh is adaptive. The basic idea is to construct a divergence-free interpolation formula for the coarse cell which is being refined. This approach works well for AMR with a refinement ratio of two. However, the interpolation polynomial can become quite complicated if the refinement ratio is larger than 2. As suggested in [4], the procedure should be applied recursively for refinement ratio of 4 or 8, and new formulae have to be derived for other refinement ratios due to the additional degrees of freedom needed to match the increased number of fine-grid faces.

In this paper, we propose a new approach that maintains the divergence-free condition with AMR. This new method is simple, can be implemented efficiently for arbitrary refinement ratios, and can be generalized to different orthogonal and curvilinear grids. In Section 2, using the CT approach, we first demonstrate how to implement our algorithm in 2D Cartesian, cylindrical and spherical grids. In Section 3, we present a few examples using this algorithm, showing its ability of maintaining divergence-free condition to high accuracy.

## 2. Algorithm

We first illustrate our algorithm using a simple 2D Cartesian grid (the generalization to 3D in Cartesian is straightforward), then move on to implementations in cylindrical and spherical grids. To simplify our

description, we assume that, for all geometries considered, each cell edge is split into equal-distance pieces according to the refinement ratio.

### 2.1. Cartesian grid

We start by first describing the approach proposed by Balsara [4], since our method is similar to his. His method was proposed originally for refinement ratios of 2 or powers of 2. Here we describe what happens when that method is used for other refinement ratios. Subplots (a), (d') and (e) in Fig. 1 show the steps. Starting with a coarse cell shown in (a), we need to refine the cell by a factor of 3 along  $x$  and 2 along  $y$ , as shown in subplot (e). First, from the known values  $u_{c0}$ ,  $u_{c1}$ ,  $v_{c0}$ ,  $v_{c1}$  of the coarse faces, one can obtain the required new quantities  $v_1$ ,  $v_2$ ,  $v_3$ ,  $v_4$ ,  $v_5$ ,  $v_6$  and  $u_1$ ,  $u_2$ ,  $u_7$ ,  $u_8$  [see subplot (d')] by using an interpolation scheme, such as a piecewise linear reconstruction on the coarse face, which is enough to achieve the second order accuracy. Note that if the coarse cell (a) shares edges with cells already refined meshes, then the field component values on those refined meshes should be copied to the new finer mesh rather than using the interpolation. In addition, to preserve the monotonicity of the coarse face values, an appropriate limiter should be used. Second, using all the fine values shown in (d') as surface boundary conditions, one can construct interpolation polynomials for  $u$  and  $v$  so that the divergence-free condition is satisfied over the whole cell (d'). Direct evaluation of the polynomials at specific positions gives the final state (e). For ease of discussion, we will refer Balsara's method as the "polynomial method" in the following.

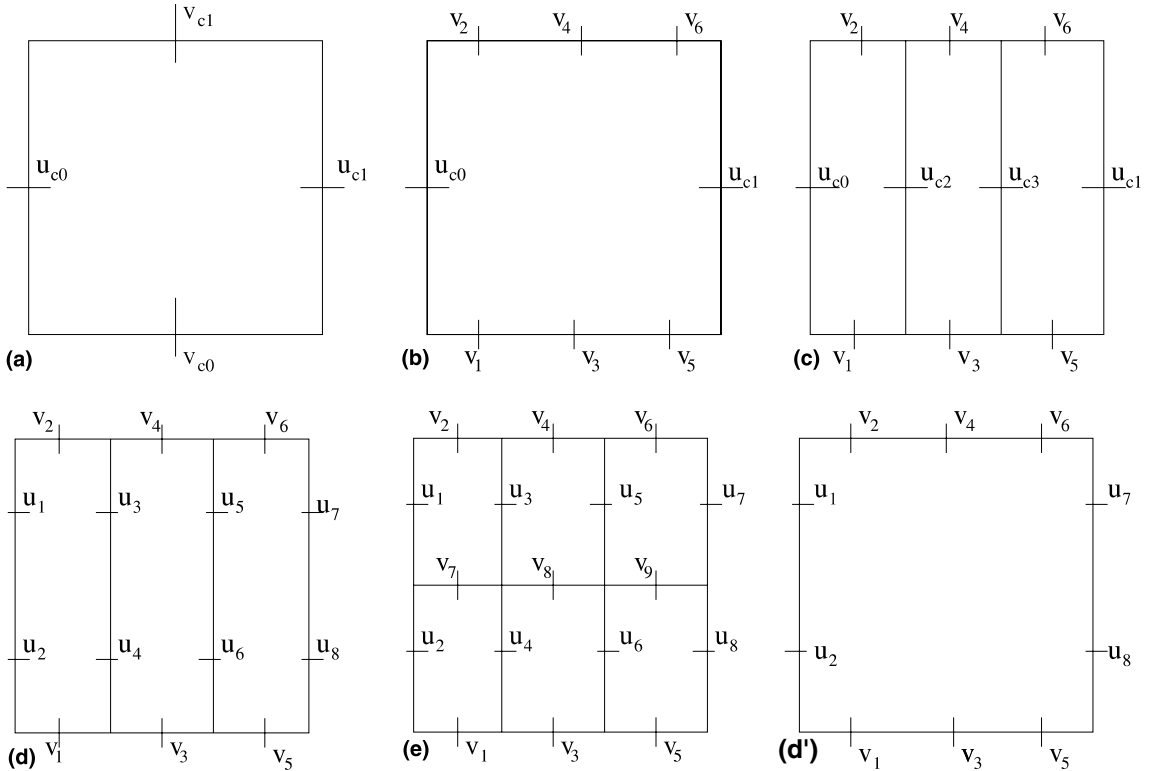


Fig. 1. Directional-splitting approach for reconstruction of the divergence-free fields on a refined grid.

As emphasized in the original paper by Balsara [4], this method is not designed for arbitrary refinement ratios. This is because calculating the appropriate polynomial while satisfying all the boundary values becomes prohibitively expensive for large degrees of freedom. Balsara's approach does give an exact method with closed-form expressions that are divergence-free and preserves the TVD property. The method, furthermore, has the property of being dimensionally unsplit.

Motivated by this method, we now propose a different algorithm which is quite simple and efficient. Our approach is illustrated in sequence by subplots (a)–(e) in Fig. 1:

- (1) We use a directional splitting approach to treat multi-dimensional problems. We first consider the refinement along the  $x$ -direction as shown in subplot (b) of Fig. 1. Obtaining boundary values  $v_1, \dots, v_6$  is the same as in Balsara's approach described above.
- (2) Given the quantities on the edges in (b), we can now partially construct the internal fine face values based on the divergence-free condition. For example, in subplot (c),  $u_{c2}$  is uniquely defined by  $u_{c0}$ ,  $v_1$ ,  $v_2$  as

$$u_{c2} = u_{c0} + (v_2 - v_1) \frac{\delta x}{\Delta y},$$

where  $\delta x$  and  $\Delta y$  are the spacings for the fine and coarse cells, respectively. The quantity  $u_{c3}$  can be calculated in the similar manner. Then, it is straightforward to show that the divergence-free condition is also preserved in the last cell by noting that

$$\frac{u_{c1} - u_{c3}}{\delta x} + \frac{v_6 - v_5}{\Delta y} = 0$$

if

$$\frac{u_{c1} - u_{c0}}{\Delta x} + \frac{\frac{1}{3}(v_2 + v_4 + v_6) - \frac{1}{3}(v_1 + v_3 + v_5)}{\Delta y} = 0.$$

- (3) We now consider the refinement along the  $y$ -direction, which is taken as two in this example. As shown in (d), quantities  $u_1$ ,  $u_2$ ,  $u_7$  and  $u_8$  can be obtained similar to step (1). In order to obtain quantities  $u_3$  and  $u_4$ , we first obtain the slope along the  $y$ -direction at  $u_{c2}$ . This limited slope can be obtained by interpolation from the known values at the left and right faces of the coarse cell  $u_{c0}$  and  $u_{c1}$ , which yields,

$$\frac{du_{c2}}{dy} = \frac{1}{3} \frac{du_{c1}}{dy} + \frac{2}{3} \frac{du_{c0}}{dy}. \quad (1)$$

Quantities  $u_3$  and  $u_4$  can then be calculated from  $u_{c2}$  and  $du_{c2}/dy$ . This step can be repeated to obtain  $u_5$  and  $u_6$ .

- (4) Quantities  $v_7$ ,  $v_8$  and  $v_9$  can be calculated using the divergence-free condition within its respective, refined cell. This is shown in (e).

Even though we have only demonstrated our algorithm in 2D, its extension to 3D should not be difficult. The interpolation on the coarse faces can be done using higher-order reconstruction as well, though it should be conservative in a finite-volume sense.

We have made detailed comparisons between our method and that by Balsara for using a refinement ratio of 2 in each direction. If the fine face values on the coarse faces are constructed in the same way and the limited slope for the intermediate coarse face is obtained via Eq. (1), we obtain exactly the same values for the internal fine faces for both 2D and 3D cases as those given by Balsara's method. This also implies that our reconstruction method has the same TVD preserving property as his method, which was discussed in [5].

The divergence-free prolongation for 3D is different from the reconstruction in [4]. The reason is that the face values of the new fine grid may come from the old fine grid, and a linear profile is not enough. Balsara [4] introduced complicated interpolation polynomials to match the known fine face values. Our results are different from Balsara's approach [4]. We may not have a closed-form expressions for the prolongation operation on a whole coarse cell. However, whenever the interpolation is needed, monotonicity-preserving linear or high-order interpolation in 1-D is used. It is efficient and TVD-preserving. We acknowledge that our approach may not be as smooth as Balsara's approach within a coarse cell.

For finite-difference and finite-volume methods on an AMR grid, a number of ghost cells are usually required at the boundary. When the number of ghost cells is not divisible by the refinement ratio, special care is needed in order to maintain the divergence-free condition in those cells. Instead, we use a virtual extended grid, where several additional zones are added. For the virtual fine grid, the number of ghost cells is divisible by the refinement ratio so that if a coarse face is next to a fine grid, it is covered wholly by the fine faces. This virtual fine grid is used only to obtain the values of fine grid whenever the grid is re-adapted. It is not used in integration.

## 2.2. Cylindrical and spherical grids

We now discuss how to implement our method in other orthogonal grids such as cylindrical and spherical coordinates with AMR. Balsara [5] has studied this issue recently as well by extending his divergence-free reconstruction of [4] to the cylindrical and spherical meshes. As described in [5], a variable substitution and coordinate transformation approach is used to transform the divergence formula of the cylindrical and spherical geometry to the standard divergence formula of the Cartesian grid. Then, the reconstruction for the Cartesian grid is applied to the new variables on the new coordinates.

We use  $(r, z, \phi)$  and  $(r, \theta, \phi)$  to represent the cylindrical and spherical coordinates, respectively. The divergence of a vector field  $\mathbf{v}$  becomes

$$\nabla \cdot \mathbf{v} = \frac{1}{r} \left( \frac{\partial(rv_r)}{\partial r} + \frac{r\partial v_z}{\partial z} + \frac{\partial v_\phi}{\partial \phi} \right), \quad (2)$$

for the cylindrical grid, and

$$\nabla \cdot \mathbf{v} = \frac{\partial(r^2 v_r)}{r^2 \partial r} + \frac{\partial(\sin \theta v_\theta)}{r \partial \theta} + \frac{\partial v_\phi}{r \sin \theta \partial \phi}, \quad (3)$$

for the spherical grid.

The main complication in implementing AMR in these geometries is to determine where the cell centers or face centers are, because they are all weighted by additional factors such as  $1/r$  and  $\sin \theta$ . In our method we assume that the edges of a grid in any direction are split into equal-distance pieces according to the refinement ratio. This typically means that the coarse cell is not divided into equal area/volume pieces.

We first discuss the cylindrical grid. The finite-volume discretization of Eq. (2) is

$$(\nabla \cdot \mathbf{v})_{i,j,k} = \frac{(r_i v_{r_i} - r_{i-1} v_{r_{i-1}})}{r_{i-\frac{1}{2}} dr} + \frac{(v_{z_j} - v_{z_{j-1}})}{dz} + \frac{(v_{\phi_k} - v_{\phi_{k-1}})}{r_{i-\frac{1}{2}} d\phi},$$

where  $r_{i-\frac{1}{2}} = \frac{1}{2}(r_i + r_{i-1})$ .

As described in Section 2.1, the reconstruction for fine cells inside a whole coarse cell begins with reconstruction on each coarse face. It can be verified that the interpolation scheme for the Cartesian grid can be applied to faces  $(z, \phi)$  for the  $v_r$  component and  $(r, z)$  for the  $v_\phi$  component, but not to face  $(r, \phi)$  for the

$v_z$  component. To construct a conservative interpolation on the face of  $(r, \phi)$ , we need to find the slopes at various intermediate points. To do this, we use a linear profile defined by

$$v_z = v_{zc} + v_{z,\phi}(\phi - \phi_0) + v_{z,r}(r - r_0), \quad (4)$$

where  $\dots, \phi, r$  stands for  $\partial/\partial\phi$  or  $\partial/\partial r$ ,  $v_{z,\phi}$  and  $v_{z,r}$  are the limited slopes, and  $(r_0, \phi_0)$  is the face center. The quantity  $v_{zc}$  is the area-averaged value of  $v_z$  on the coarse face  $[r_{i-1}, r_i] \times [\phi_{k-1}, \phi_k]$ , which is defined by

$$v_{zc} = \frac{1}{\int \int r dr d\phi} \int_{r_{i-1}}^{r_i} \int_{\phi_{k-1}}^{\phi_k} v_z r dr d\phi. \quad (5)$$

Inserting (4) into (5) and simplifying it, we obtain

$$v_{z,\phi}(\phi_{k-\frac{1}{2}} - \phi_0) + v_{z,r} \left( \frac{2(r_i^3 - r_{i-1}^3)}{3(r_i^2 - r_{i-1}^2)} - r_0 \right) = 0. \quad (6)$$

To satisfy Eq. (6), we let

$$\phi_0 = \phi_{k-\frac{1}{2}} = \frac{1}{2}(\phi_k + \phi_{k-1}), \quad (7)$$

$$r_0 = \frac{2(r_i^3 - r_{i-1}^3)}{3(r_i^2 - r_{i-1}^2)}. \quad (8)$$

We should mention that the expression for  $\phi_0$  and  $r_0$  are also valid for faces on a fine grid. Therefore, when the mesh is refined with ratio  $m$ , face centers for the fine mesh can be calculated in the same fashion. Let  $\delta r = (r_i - r_{i-1})/m$  and  $r = r_i$ , then the face centers for the fine grid will be

$$r_{0l} = \frac{2[(r - l\delta r)^3 - (r - (l+1)\delta r)^3]}{3[(r - l\delta r)^2 - (r - (l+1)\delta r)^2]}, \quad l = 0, 1, \dots, m-1.$$

After all the face centers are calculated, the vector field components can be calculated by the linear profile (4), for example, in  $r$ -direction,

$$v_{z0l,k} = v_{zc} + v_{z,r}(r_{0l} - r_0).$$

If we denote the area for the fine and coarse faces by

$$dA_{0l} = \frac{1}{2}(r_{0(l+1)}^2 - r_{0l}^2) d\phi, \quad dA_c = \frac{1}{2}(r_k^2 - r_{k-1}^2) d\phi,$$

then it can be verified that

$$\sum_{l=0}^{m-1} v_{z0l,k} \cdot dA_{0l} = v_{zc} \cdot dA_c,$$

which means the flux is conserved after interpolation.

The face reconstruction for AMR on spherical grid is more complicated than the cylindrical case because all faces need to be constructed specially. Take a reduced 2-D problem  $(r, \theta)$  as an example. (The full 3-D case can be derived similarly.) The divergence condition becomes

$$\nabla \cdot \mathbf{v} = \frac{1}{r^2} \frac{\partial(r^2 v_r)}{\partial r} + \frac{1}{r \sin \theta} \frac{\partial(\sin \theta v_\theta)}{\partial \theta}. \quad (9)$$

Integrating (9) on cell  $[r_{i-1}, r_i] \times [\theta_{j-1}, \theta_j]$ , we obtain

$$\nabla \cdot \mathbf{v} = \frac{1}{\Delta V} ((v_{r_i} r_i^2 - v_{r_{i-1}} r_{i-1}^2)(\cos \theta_{j-1} - \cos \theta_j) + v_{\theta_j} r_{i-\frac{1}{2}} \sin \theta_j \, dr - v_{\theta_{j-1}} r_{i-\frac{1}{2}} \sin \theta_{j-1} \, dr), \quad (10)$$

where  $\Delta V = \frac{1}{3}(r_i^3 - r_{i-1}^3)(\cos \theta_{j-1} - \cos \theta_j)$  (where we drop  $d\phi$  in our expressions) is the cell volume. Note that  $dA_\theta = r_i^2(\cos \theta_{j-1} - \cos \theta_j)$  is the area of the  $(\theta, \phi)$  face at  $r = r_i$  and  $dA_r = r_{i-\frac{1}{2}} \sin \theta_j \, dr$  is the area of the  $(r, \phi)$  face at  $\theta = \theta_j$ , the discretization is in good agreement with the physical definition of the divergence.

To do the reconstruction of a vector  $\mathbf{v}$  on a coarse face, we define  $v_r$  as the field component at cell's  $(\theta, \phi)$  face,  $v_\theta$  at cell's  $(r, \phi)$  face. A piecewise linear profile via a slope limiter for  $v_r$  and  $v_\theta$  can be constructed in the same way as for the Cartesian grid. Assume that the limited slope for  $v_r$  in  $\theta$  direction is  $v_{r,\theta}$  and the linear profile is

$$v_r = v_{r_c} + v_{r,\theta}(\theta - \theta_0),$$

where  $\theta_0$  is the center for the coarse  $(\theta, \phi)$  face. Unlike in Cartesian or cylindrical coordinates, however,

$$\theta_0 \neq \frac{1}{2}(\theta_j + \theta_{j-1})$$

in spherical coordinates. Instead, we define  $v_{r_c}$  as

$$\frac{1}{r(\cos \theta_{j-1} - \cos \theta_j)} \int_{\theta_{j-1}}^{\theta_j} v_r \cdot r \sin \theta \, d\theta = v_{r_c},$$

which yields

$$\theta_0 = \frac{\theta_{j-1} \cos \theta_{j-1} - \theta_j \cos \theta_j + \sin \theta_j - \sin \theta_{j-1}}{\cos \theta_{j-1} - \cos \theta_j}.$$

Similarly, for  $v_{\theta,r}$ , we use the linear profile

$$v_\theta = v_{\theta_c} + v_{\theta,r}(r - r_0),$$

where  $r_0$  is the center of the coarse  $(r, \phi)$  face. Then, we have

$$\int_{r_{i-1}}^{r_i} (r - r_0) r \sin \theta \, dr = 0,$$

which yields

$$r_0 = \frac{2(r_i^3 - r_{i-1}^3)}{3(r_i^2 - r_{i-1}^2)},$$

the same as (8). After all the face centers are calculated, the vector field components can be calculated by the linear profile, as we have done for the cylindrical grid.

At the origin  $r = 0$ , we have only three faces, so we do not need the value of  $v_r$  at the origin. At  $\theta = 0$  or  $\theta = \pi$ , we also have only three faces, and the reconstruction of  $v_\theta$  needs special treatment. Since  $dA_r = r_{i-\frac{1}{2}} \sin \theta_j = 0$  at  $\theta = 0$  or  $\pi$ , we re-define  $dA_r = \Delta r$ , which is reduced to the reconstruction on a uniform 1-D grid. If the new fine grid shares face with the old fine grid, we do not need to construct the linear profile for the coarse face and only copy the values of the old fine grid to the new grid.

After the face reconstruction is finished, the algorithm described in Section 2.1 can be used to reconstruct the internal faces step by step.

In principle, our algorithm can also be applied to general structured curvilinear grids and unstructured triangle meshes.

### 3. Numerical experiment

We have implemented our algorithm in our MHD AMR solver [14]. In addition, we have implemented Balsara's electrical force correction method [4] to ensure that the restriction from fine to coarse grids preserves the divergence-free condition of magnetic fields. In this section, we present several 2D numerical examples in Cartesian, cylindrical and spherical geometries. In all the cases, magnetic field components are defined at the edge/face centers while all other fluid quantities are defined at the cell centers. A second-order Roe's Riemann solver is used to advance the conservative variables.

#### 3.1. Examples for Cartesian geometry

The first example is originally from Brio and Wu [6]. It is a classical 1-D shock-tube problem but we solve it as a 2-D problem in the  $\{x, y\}$  plane with an angle  $\alpha$  between the shock front and the  $y$ -axis. Since this test with  $\alpha = 45^\circ$  has been solved by Jiang and Wu [12] and many others, we choose  $\alpha = \tan^{-1} 2 \approx 63.4^\circ$ . The initial states are

$$(\rho, v_{\parallel}, v_{\perp}, p, B_{\perp}, B_z, p) = \begin{cases} (1, 0, 0, 0, 1, 0, 1), & \text{left,} \\ (0.125, 0, 0, 0, -1, 0, 0.1), & \text{right,} \end{cases}$$

where  $\parallel$  refers to the direction along the normal of the shock front,  $\perp$  refers to the direction perpendicular to the normal of the shock front but still in the computational plane and  $z$  refers to the direction out of the plane. The value  $B_{\parallel}$  is taken as 0.75.

Since the magnetic field is not uniform initially, it is important to make the initial condition satisfy  $\nabla \cdot \mathbf{B} = 0$ . We first obtained the potential field  $\mathbf{A}$  at each node from the given value of magnetic field  $B_{\parallel}$  and  $B_{\perp}$ . Then, the  $B_x$  and  $B_y$  at the cell-interfaces are obtained via the central differencing of  $\mathbf{A}$ .

As suggested by Tóth [18], the computational domain can be set up as a narrow strip  $[0, 1] \times [0, 2/N]$ , discretized with an  $N \times 2$  grid. Grid spacing is chosen as  $\Delta x = \Delta y$ . The top and bottom boundaries are specified by imposing the continuity of all variables along the traverse direction  $\eta = y \cos \alpha - x \sin \alpha$ , while the left and right boundaries are fixed according to the initial conditions. The computation is stopped at time  $t = 0.1 \cos \alpha = 0.1/\sqrt{5}$ . We first solved it with  $N = 400$  without refinement and then solved it with  $N = 200$  and a two-level refinement with a refinement ratio of 2.

The numerical results are shown in Fig. 2. It is clearly seen that the AMR results coincide very well with the uniform grid with the same resolution. The average L1 error between the 400 uniform grid and two-level AMR grid is  $2.23\text{e} - 5$ .

As pointed out by Tóth [18], the conservation of  $B_{\parallel}$  is accurate only to truncation errors at best for general  $\alpha$ , although the divergence-free condition is accurate to machine round-off error. From Fig. 2, we can see that the AMR process does not amplify the truncation error of  $B_{\parallel}$ . A constant  $B_{\parallel}$  can be maintained, however, if one uses a grid ratio  $\Delta x/\Delta y = \tan \alpha$ .

The next example is taken from Dai and Woodward [7]. It models the disruption of a high density cloud by a strong shock wave. The computational domain is  $\{x, y\} = [0, 1] \times [0, 1]$ . The initial condition contains a discontinuity parallel to the  $y$ -axis at  $x = 0.6$  with the left and right states

$$(\rho, v_x, B_y, B_z, p) = \begin{cases} (3.86859, 0, 2.1826182, -2.1826182, 167.345), & \text{left,} \\ (1, -11.2536, 0.56418958, 0.56418958, 1), & \text{right} \end{cases}$$

and  $v_y = v_z = B_x = 0$ . The circular cloud is located initially at  $x = 0.8$ ,  $y = 0.5$  with a radius 0.15, density  $\rho = 10$ . There is a fixed boundary condition on the right at  $x = 1$  due to the supersonic flow, while the other boundaries are approximately open with out-flow boundary conditions. An adiabatic equation of state with an index  $\gamma = 5/3$  is used.



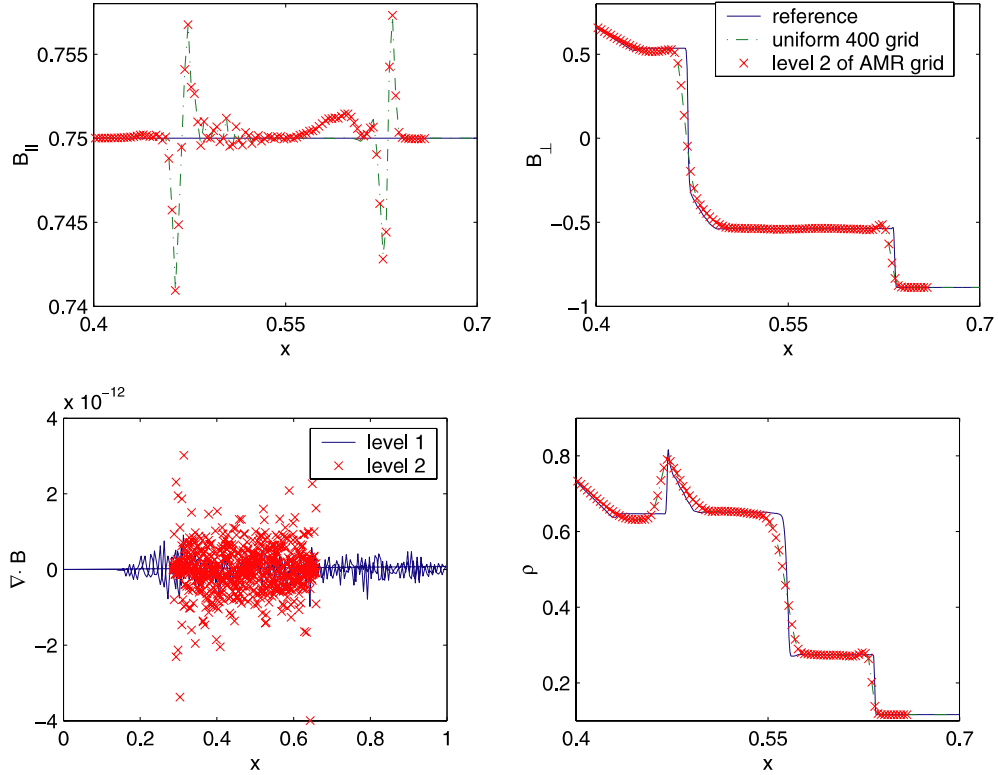


Fig. 2. Results for the oblique shock-tube problem of Brio and Wu [6] with  $\alpha = \tan^{-1} 2$ . The output time is  $t = 0.1/\sqrt{5}$ .

We tested this example with different refinement ratios. The base grid we used is  $100 \times 100$ . The density contour plots with refinement and  $\nabla \cdot \mathbf{B}$  at  $t = 0.06$  are plotted in Figs. 3(a)–(d).

### 3.2. Examples for cylindrical geometry

We tested our algorithm for cylindrical geometry with two examples. The first one is a 2-D problem first introduced in [2], where it was solved in a Cartesian grid. We reformulated it using cylindrical geometry. The computational domain is a disk with  $(r, \phi) = [0, 0.6] \times [0, 2\pi]$ . A dense disk of fluid with  $\rho = 10$  and radius  $r_0 = 0.1$  is rotating around the  $r = 0$  axis with  $v_\phi = 20r$ . The ambient fluid is at rest with  $\rho = 1$ . An adiabatic equation of state with an index  $\gamma = 5/3$  is used.

The initial magnetic field is uniform with  $B_x = 5/\sqrt{4\pi}$  and  $B_y = 0$ , where  $x$  is along  $\phi = 0$ . Converting these into cylindrical coordinates, we have

$$\begin{aligned} B_r &= B_x \cos \phi, \\ B_\phi &= -B_x \sin \phi, \end{aligned} \tag{11}$$

which is not divergence-free in our finite-volume discretization. Therefore, we adopted an approximate initialization for  $B_r$ , which is

$$B_r = B_x \frac{\sin \phi_{j+1} - \sin \phi_j}{d\phi}.$$

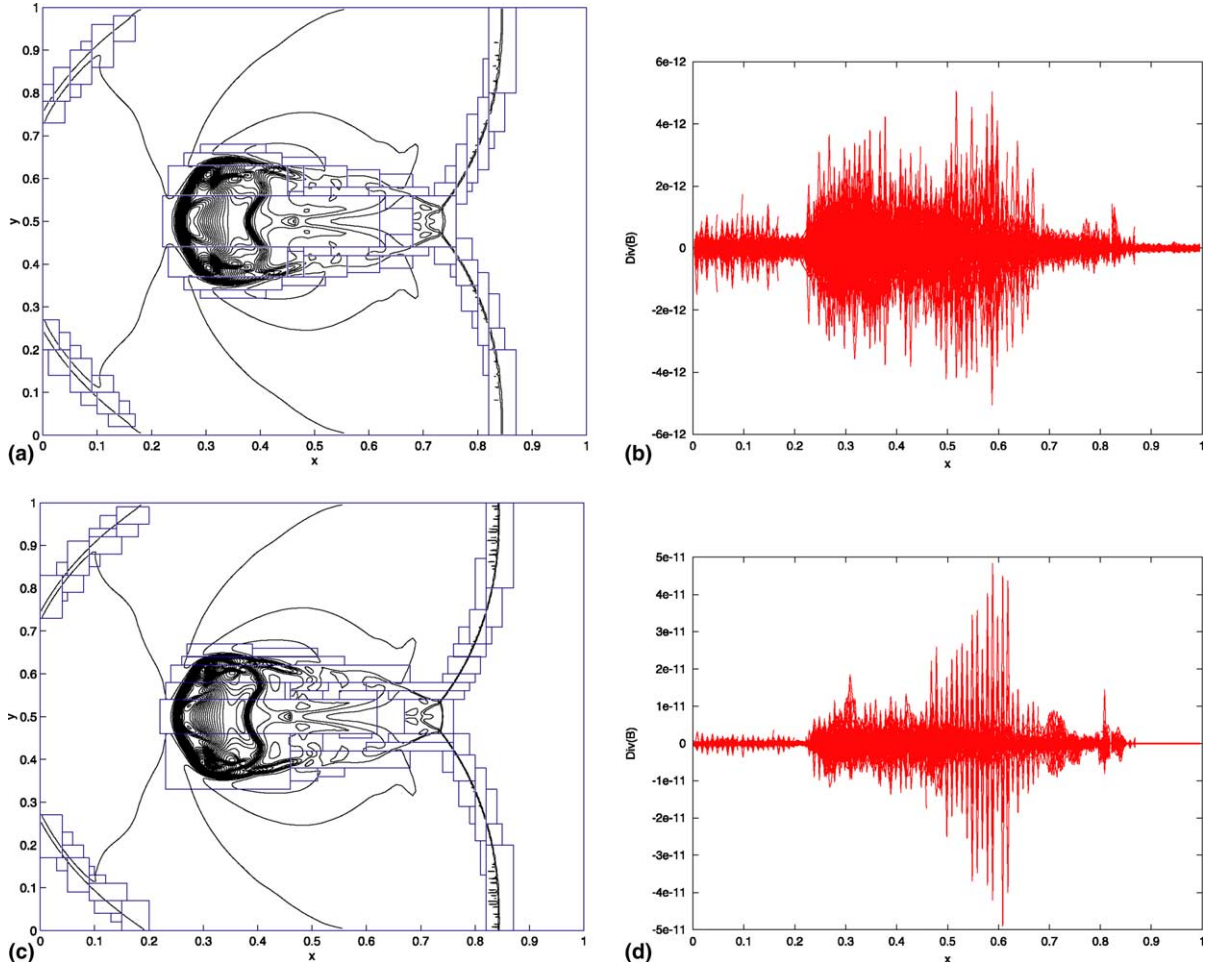


Fig. 3. (a) The density contour plot and refinement with refinement ratio of 2 at  $t = 0.06$  for cloud–shock interaction problem. Forty four contours from 1 to 44 are used. (b) The  $\nabla \cdot \mathbf{B}$  at  $t = 0.06$  for (a). At each  $x$ , values of  $\nabla \cdot \mathbf{B}$  at different  $y$  are plotted. (c) The density contour plot and refinement with refinement ratio of 3 at  $t = 0.06$  for cloud–shock interaction problem. Forty four contours from 1 to 44 are used. (d) The  $\nabla \cdot \mathbf{B}$  at  $t = 0.06$  for (c). At each  $x$ , values of  $\nabla \cdot \mathbf{B}$  at different  $y$  are plotted.

This problem has two challenges for preserving the divergence-free condition on an AMR grid. The first is the singular point at the origin. For the  $B_r$  component, although it is not used in our finite-volume discretization for calculating  $\nabla \cdot \mathbf{B}$  (it is canceled due to the zero area at  $r = 0$ ), it is needed in calculating the cell-centered values of  $B_r$ , which is then used in the Riemann solver. To calculate the  $dB_r/dt$  at the origin, we use extrapolation based on the cell-centered values of  $dB_r/dt$  at  $(\phi, \frac{1}{2}dr)$  (which is calculated by our Riemann solver) and the values at  $r_1 = dr$ .

For obtaining the  $B_\phi$  component at  $r = 0$ , the Riemann solver produces different electric-field values for different  $\phi$  at the origin. To maintain the divergence-free condition, only one electric-field value at the origin should be used to advance the  $B_\phi$  for all of the  $\phi$ s. We set the electric-field at the origin to be the average over the whole circle.

The next challenge is the periodic boundary condition in  $\phi$ . Every patch that shares an edge with  $\phi = 0$  or  $\phi = 2\pi$  can become potentially an electric-field correction partner for a coarse patch on the other end. It

is important to make sure that the correction does only once for each cell, and the  $B_\phi$  and the electric-field components have the same values (up to the round-off error) at  $\phi = 0$  and  $\phi = 2\pi$ .

We use three refinement levels for this example. The refinement ratio is 3 and 2, respectively. The base grid is  $60 \times 60$ . As suggested in [2], we output the solution at time  $t = 0.295$ . Figs. 4(a)–(d) show the results at time  $t = 0$  and  $t = 0.295$ . For comparison, we have run this problem in Cartesian coordinates with a base grid of  $100 \times 100$  and the same refinement levels and ratios. The density contours from these two runs are shown in Figs. 5(a) and (b), respectively.

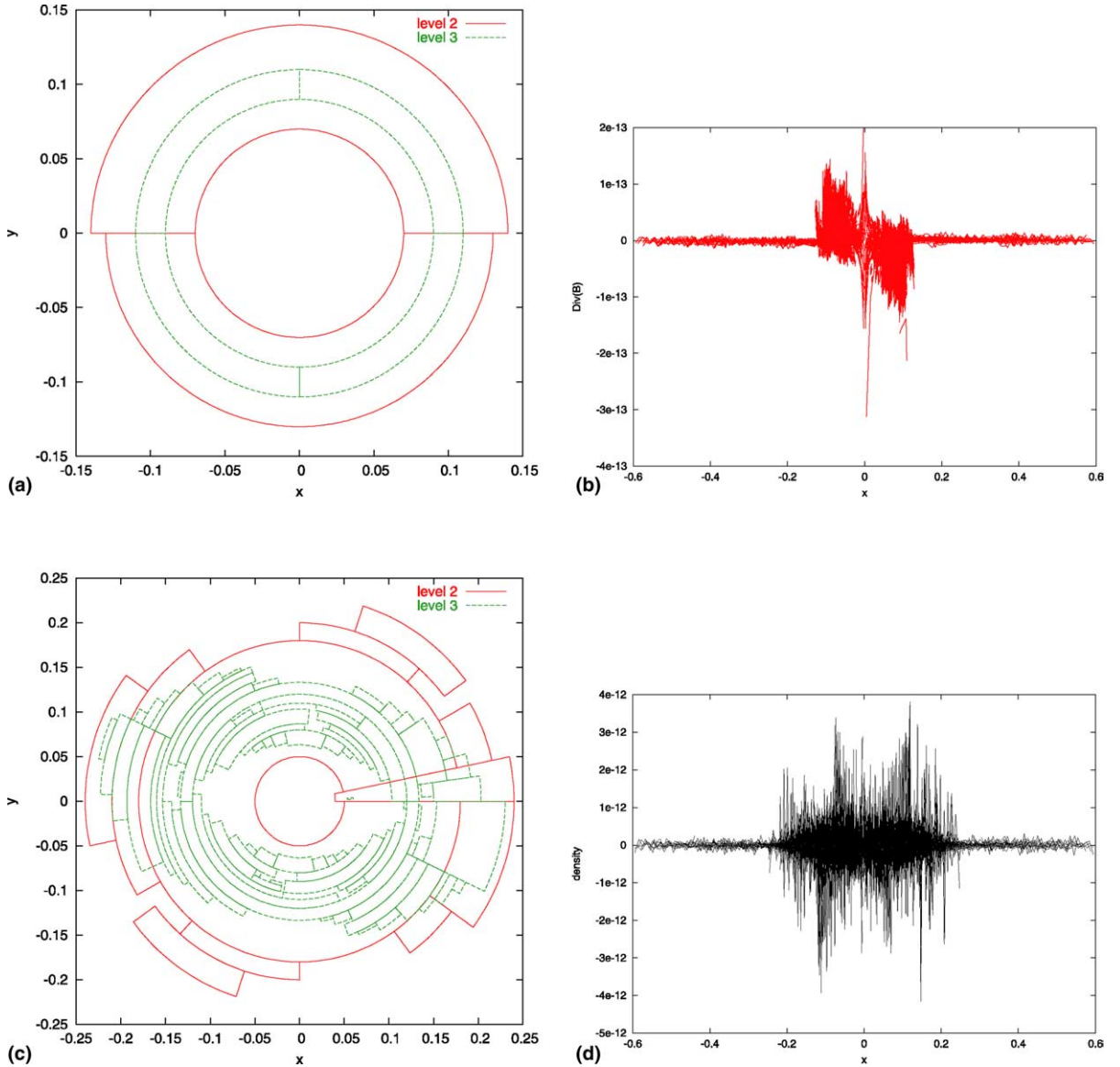


Fig. 4. (a) The initial refinement at  $t = 0$ . (b) The initial  $\nabla \cdot \mathbf{B}$  at  $t = 0$  for (a). At each  $x$ , values of  $\nabla \cdot \mathbf{B}$  at different  $y$  are plotted. (c) The refinement at  $t = 0.295$ . The refinement ratios are 3 and 2, respectively. (d) The  $\nabla \cdot \mathbf{B}$  at  $t = 0.295$  for (c). At each  $x$ , values of  $\nabla \cdot \mathbf{B}$  at different  $y$  are plotted.

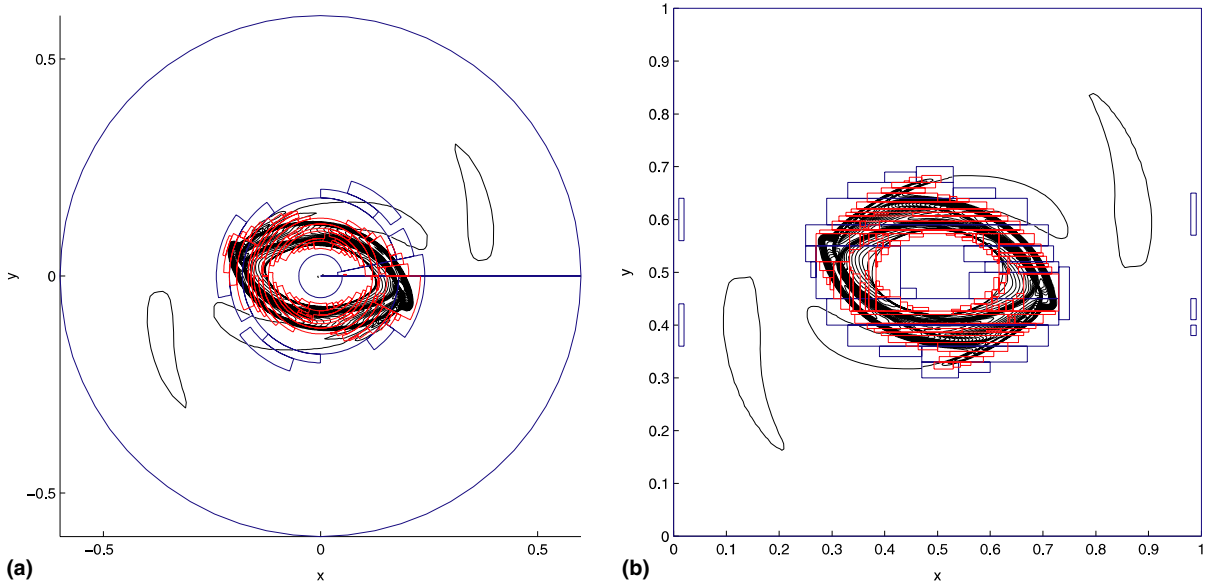


Fig. 5. (a) Density contour plots with three-level refinement for rotor problem.  $t = 0.295$ . Thirty contour-lines between 0.532 and 10.83 are used. (b) Density contour plots with three-level refinement for rotor problem  $t = 0.295$ . Thirty contour-lines between 0.532 and 10.83 are used. The results were obtained by Cartesian grid method with base grid  $100 \times 100$  and three-refinement levels.

The second example is in the  $(r, z)$  coordinates. It was introduced in [17]. The problem is simulating a light cylindrical MHD jet with a top-hat velocity profile propagating through a background medium. We used a computation domain  $(r, z) = [0, 1] \times [0, 2]$ . The base grid is  $200 \times 200$ . The jet has a radius  $r = 0.125$  initially, which is about 25 base grid cells. The jet has an initial Mach number of 20, a gas density contrast between the jet and ambient medium of  $\rho_{\text{jet}}/\rho_{\text{amb}} = 0.1$ . The ambient medium has a sound speed of 1, and an initial ambient magnetic field of  $B_\phi = B_r = 0$  and  $B_z = B_{\text{amb}} = 0.1$ . The jet carries a helical magnetic field with  $B_r = 0$ ,  $B_\phi = 2B_{\text{amb}}(r/r_{\text{jet}})$  and  $B_z = B_{\text{amb}}$ .

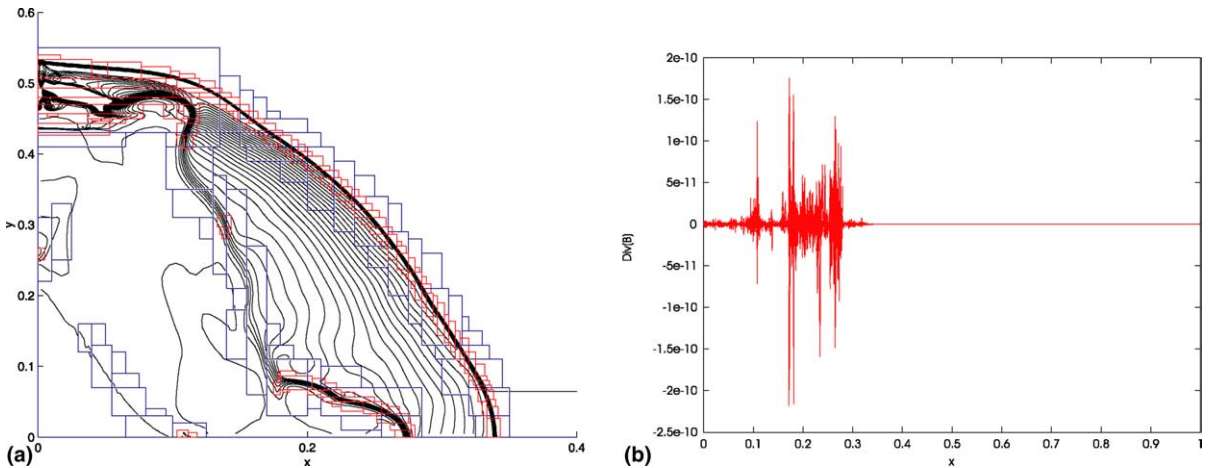


Fig. 6. (a) The “zoomed” version of refinement and density contour plot for the jet problem on cylindrical  $(r, z)$  plane. (b) The  $\nabla \cdot \mathbf{B}$  for (a). At each  $r$ , values of  $\nabla \cdot \mathbf{B}$  at different  $z$  are plotted.

We again used three levels of refinement with refinement ratios of 3 and 2. We ran our simulation until  $t = 0.1$ . Fig. 6(a) shows the density contour plot with refinement. Fig. 6(b) shows the results of  $\nabla \cdot \mathbf{B}$ .

### 3.3. An example for spherical geometry

The last example is on simulating a rising buoyant bubble in an isothermal background gas, which is initially in a pressure equilibrium under an external gravitational field. Its density (and pressure) profile is described as  $\rho = p = \exp(-r)$ . A spherical bubble with a radius 0.5 is initially located at (1.1, 0). At  $t = 0$ ,

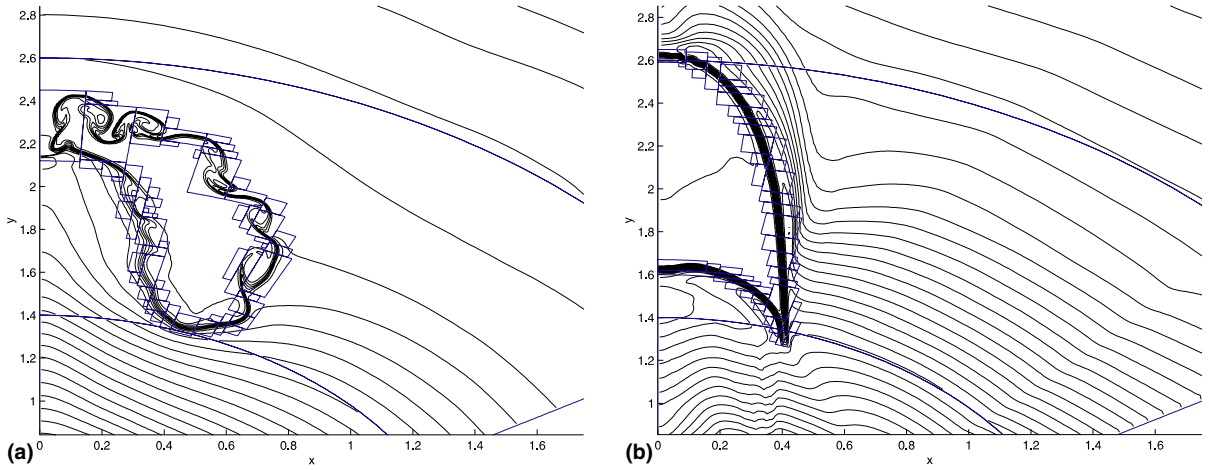


Fig. 7. (a) The density contour plot with refinement for bubble problem with no magnetic field. (b) The density contour plot with refinement for bubble problem with strong magnetic field  $b = 0.4$ .

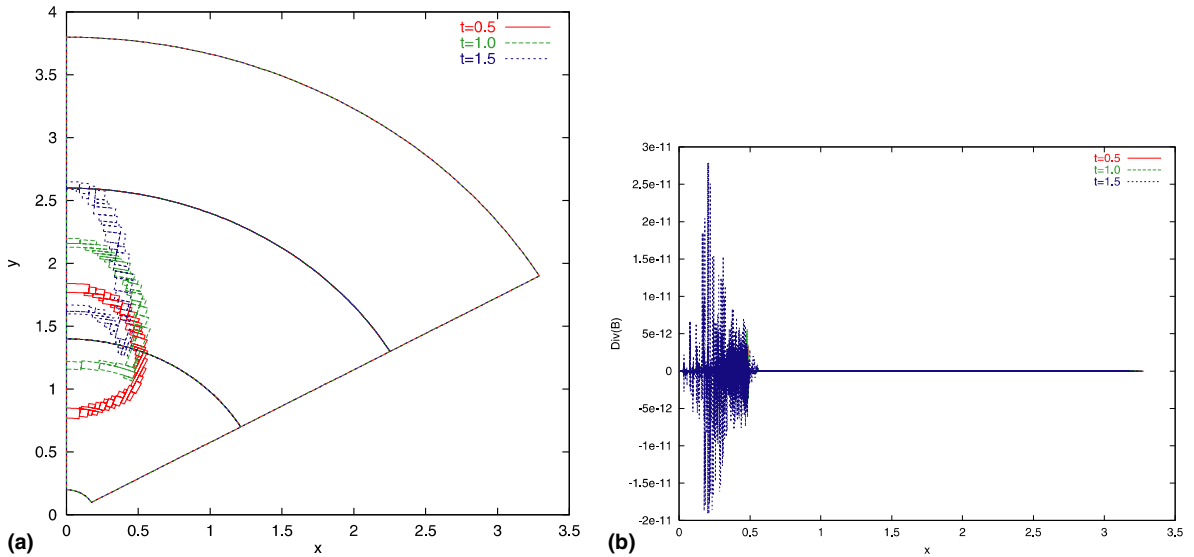


Fig. 8. (a) The refinement at different times in an axis-symmetric spherical grid. (b) The  $\nabla \cdot \mathbf{B}$  for (a). Again, values at all cells and three different times are plotted.

the density inside the bubble is taken as  $\rho = 0.1 \exp(-r)$ , so that the bubble will rise due to the pressure imbalance. (Some details are further described in [14]).

The computational domain in  $(r, \theta)$  is  $[0.2, 3.8] \times [0, \pi/3]$ . We first simulated this problem without any external magnetic field, i.e.,  $B_r = B_\theta = B_\phi = 0$ , and observed the Rayleigh–Taylor instability at the contact interface (see Fig. 7(a)). We then used a uniform magnetic field along the  $z(=r \cos \theta)$  direction. It is a potential field with magnitude  $F = -b \cdot r \cos \theta$ . The magnetic field is defined by

$$\mathbf{B} = -\nabla F = (b \cos \theta, -b \sin \theta),$$

where the constant  $b$  controls the magnitude of the magnetic field. We simulated this problem with  $b = 0.4$ . The Rayleigh–Taylor instability at the contact interface is suppressed by the strong magnetic field (see Fig. 7(b)).

We used a base grid of  $360 \times 120$  and a refinement ratio of 3. The refinements at different times are shown in Fig. 8(a). The divergence of the magnetic field is shown in Fig. 8(b).

## Acknowledgements

We thank Burt Wendroff for useful discussion. This research was performed under the auspices of the Department of Energy. It was supported by the Laboratory Directed Research and Development Program at Los Alamos. The authors also thank the referees' comments which help us to improve the clarification of the paper.

## References

- [1] M.J. Berger, P. Colella, Local adaptive mesh refinement for shock hydrodynamics, *J. Comput. Phys.* 82 (1989) 64–84.
- [2] D.S. Balsara, D.S. Spicer, A staggered mesh algorithm using high order Godunov fluxes to ensure solenoidal magnetic fields in magnetohydrodynamics simulations, *J. Comput. Phys.* 149 (1999) 270–292.
- [3] J.U. Brackbill, D.C. Barnes, The effect of nonzero  $\nabla \cdot \mathbf{B}$  on the numerical solution of the magnetohydrodynamic equations, *J. Comput. Phys.* 35 (1980) 426.
- [4] D.S. Balsara, Divergence-free adaptive mesh refinement for magneto-hydrodynamics, *J. Comput. Phys.* 174 (2001) 614–648.
- [5] D.S. Balsara, Second order accurate schemes for magnetohydrodynamics with divergence-free reconstruction. Available from: astro-ph/0308249, (2003).
- [6] M. Brion, C.C. Wu, An upwinding differencing schemes for the equations for ideal magnetohydrodynamics, *J. Comput. Phys.* 75 (1988) 400.
- [7] W. Dai, P.R. Woodward, A simple finite difference scheme for multidimensional magnetohydrodynamics, *J. Comput. Phys.* 142 (1998) 331–369.
- [8] C.R. DeVore, Flux corrected transport techniques for multidimensional compressible magnetohydrodynamics, *J. Comput. Phys.* 92 (1992) 142.
- [9] A. Dedner, F. Kemm, D. Kroner, C.D. Munz, T. Schnitzer, M. Wesenberg, Hyperbolic divergence-cleaning for the MHD equations, *J. Comput. Phys.* 175 (2002) 645.
- [10] C.R. Evans, J.F. Hawley, Simulation of magnetohydrodynamic flows: a constrained transport method, *Astrophys. J.* 332 (1989) 659.
- [11] P. Janhunen, A positive conservative method for magnetohydrodynamics based on HLL and Roe methods, *J. Comput. Phys.* 160 (2000) 649.
- [12] G.S. Jiang, C.-C. Wu, A high-order WENO finite difference scheme for the equations of ideal magnetohydrodynamics, *J. Comput. Phys.* 150 (1999) 561–594.
- [13] P. Londrillo, L. Del Zanna, High-order upwinding schemes for multidimensional magnetohydrodynamics, *Astrophys. J.* 530 (2000) 508.
- [14] S. Li, H. Li, A modern code for solving magnetohydrodynamics or hydrodynamic equations, Technical Report, Los Alamos National Laboratory, LA-UR-03-8926, 2003.
- [15] K.G. Powell, An approximate Riemann solver for MHD (that actually works in more than one dimension), Technical Report N0. 94-24, ICASE, Langley VA, 1994.

- [16] K.G. Powell, P.L. Roe, T.J. Linde, T.I. Gombosi, D.L. DeZeeuw, A solution-adaptive upwinding scheme for ideal magnetohydrodynamics, *J. Comput. Phys.* 154 (1999) 284.
- [17] D. Ryu, F. Miniati, T.W. Jones, A. Frank, A divergence-free upwinding code for multi-dimensional MHD flows, *Astrophys. J.* 509 (1998) 244–255.
- [18] G. Tóth, The  $\nabla \cdot \mathbf{B} = 0$  constraint in shock-capturing magnetohydrodynamics codes, *J. Comput. Phys.* 161 (2000) 605–652.
- [19] G. Tóth, P.L. Roe, Divergence- and curl-preserving prolongation and restriction formulas, *J. Comput. Phys.* 180 (2002) 736–750.
- [20] K.S. Yee, Numerical solution of initial boundary value problems involving Maxwell's equation in an isotropic media, *IEEE Trans. Antenna Propag.* AP-14 (1966) 302.